Physical properties of Ce$_{3+x}$Ru$_4$Sn$_{13-x}$ single crystals

Jeonghun Lee● and Eundeok Mun●

Department of Physics, Simon Fraser University, 8888 University Dr, Burnaby, BC V5A 1S6, Canada

Single crystals of Ce$_{3+x}$Ru$_4$Sn$_{13-x}$ ($0.05 \leqslant x \leqslant 0.34$), which adopt the cubic structure ($Pm\bar{3}n$, No. 223), have been grown with Sn flux. Thermodynamic and transport property measurements from single-crystal samples do not show any sign of magnetic ordering down to 1.8 K and indicate coexistence of the Kondo effect and crystalline electric field effect. The local minimum in the electrical resistivity and highly enhanced specific heat values at low temperatures characterize this family as a heavy fermion Kondo lattice system. A broad peak is observed at ∼3.5 K for $x = 0.05$ in the specific heat and magnetic susceptibility, suggesting a significant Kondo contribution, and the peak disappears as x increases. The evolution of physical properties of Ce$_{3+x}$Ru$_4$Sn$_{13-x}$ compounds can be attributed to the nature of the individual Ce ions that occupy two inequivalent 2a and 6d crystallographic sites.

I. INTRODUCTION

The intermetallic compounds with a nominal stoichiometry $R_3T_4X_{13}$ (R = rare-earth or alkaline earth, T = transition metal, and X = p-block element) crystallize into the cubic Yb$_3$Rh$_4$Sn$_{13}$-type structure ($Pm\bar{3}n$) [1,2] and show diverse phenomena such as superconductivity [3], heavy fermion behavior [4], and charge-density-wave transition [5,6]. In addition, some Ce- and Yb-based $R_3T_4X_{13}$ compounds such as Ce$_3$Rh$_4$Sn$_{13}$ and Yb$_3$Ir$_4$Ge$_{13}$ show complex magnetic behavior with no clear signature of long-range magnetic order [7,8]. In the Yb$_3$Rh$_4$Sn$_{13}$-type structure, a tilted three-dimensional network of corner-sharing Rh(Sn)$_6$ trigonal prisms forms the backbone of the crystal structure and two large cavities in cuboctahedra and icosahedra arrangements are filled by Yb (Wyckoff position 6d) and Sn (Wyckoff position 2a), respectively [9]. In some $R_3T_4X_{13}$ (3-4-13) compounds, the X atoms at the 2a site can be substituted by R atoms [10,11], leading to the chemical formula $R_{3+x}T_4X_{13-x}$, where x is the occupancy of R at the 2a site. When the X atoms at the 2a site are fully substituted by R atoms (e.g., $x = 1$), compounds are known to adopt the cubic LaRuSn$_3$-type (1-1-3) structure ($Pm\bar{3}n$) [10]. For example, RPtIn$_3$ [12], CeRuGe$_3$ [13], RRhSn$_3$ [14], and RRuSn$_3$ [10] adopt the LaRuSn$_3$-type structure. However, in these compounds, the mixed occupancy at the 2a site has been observed and their 3-4-13 counterparts ($x = 0$) are also reported. Therefore the general formula $R_{3+x}T_4X_{13-x}$ can be used to describe the type of structure in this family of compounds.

Although the 3-4-13 ($x = 0$) and 1-1-3 ($x = 1$) compounds belong to the same space group $Pm\bar{3}n$, their observed physical properties show significant differences mostly due to the replacement of X atoms by R atoms at the 2a site. For example, the compound Ce$_3$Rh$_4$Sn$_{13}$ reveals no magnetic ordering down to 50 mK [15], whereas the compound CeRhSn$_3$ shows typical Kondo lattice behavior with a magnetic phase transition at 4 K [14]. The electrical

resistivity of La$_3$Rh$_4$Sn$_{13}$ follows metallic behavior [7,16,17], but LaRhSn$_3$ shows semiconductorlike behavior [14]. The heavy fermion Ce$_{3+x}$Ru$_4$Sn$_{13-x}$ system also shows a strong x-dependence in their physical properties [18,20–22]. At low temperatures, the specific heat divided by temperature, C/T, of Ce$_3$Ru$_4$Sn$_{13}$ shows a diverging behavior as temperature decreases, reaching a value as high as 4 J mol$_{Ce}^{-1}$ K^{-2} at $T = 0.4$ K [18], while C/T of CeRuSn$_3$ shows a broad maximum at $T \sim 0.6$ K with a value of 1.5 J mol$_{Ce}^{-1}$ K^{-2} [22]. The magnetic susceptibility measurement of CeRuSn$_3$ also indicates a broad maximum at $T \sim 0.6$ K [22], where the origin of the maximum is suggested to be short-range magnetic fluctuations and (or) spin-glass dynamics [19,22]. The electrical resistivity measurements of these compounds also show a clear distinction in that Ce$_3$Ru$_4$Sn$_{13}$ follows metallic Kondo lattice behavior [18] and CeRuSn$_3$ shows semiconductorlike behavior [22].

In this report, we demonstrate that physical properties of the Ce$_{3+x}$Ru$_4$Sn$_{13-x}$ system are very sensitive to the initial Ce/Sn loading compositions, eventually controlling the Ce occupancy at the 2a site. In order to control the occupancy of Ce at the 2a site, single crystals of Ce$_{3+x}$Ru$_4$Sn$_{13-x}$ ($0.05 \leqslant x \leqslant 0.34$) have been grown with Sn flux with various Ce/Sn ratios. A systematic variation of thermodynamic and transport properties is clearly observed as x increases from 0.05 to 0.34. The observed physical properties for the $x = 0.05$ and 0.34 single crystals are quite similar to those of earlier polycrystalline Ce$_3$Ru$_4$Sn$_{13}$ and CeRuSn$_3$ results, respectively.

II. EXPERIMENTS

Single crystals of Ce$_{3+x}$Ru$_4$Sn$_{13-x}$ ($0.05 \leqslant x \leqslant 0.34$) were prepared with different initial Ce, Ru, and Sn ratios. High-purity Ce, Ru, and Sn were loaded into alumina crucible with the ratios described in Table I. The crucibles were sealed into amorphous silica tubes under partial Argon atmosphere.

TABLE I. Summary of single-crystal growth conditions and parameters obtained from EDX and XRD.

No.	ILC[a]			TP[b]	EDX[c] (at. %)			$R_{3+x}Ru_4Sn_{13-x}$.	LP[d]	Phase
	Ce	Ru	Sn		Ce	Ru	Sn	x	a (Å)	
0	3	5	92	(1190, 900, 3)						Ru_3Sn_7
1	3.75	5	91.25	(1200, 950, 1)	14.3(2)	18.7(4)	67.0(6)	0.05(6)	9.7326(16)	$Ce_{3+x}Ru_4Sn_{13-x}$
2	5	5	90	(1190, 900, 3)	14.6(2)	18.8(2)	66.6(1)	0.12(3)	9.7302(16)	$Ce_{3+x}Ru_4Sn_{13-x}$
3	7.5	5	80.75	(1190, 900, 3)	14.9(3)	18.5(2)	66.6(5)	0.18(4)	9.7299(12)	$Ce_{3+x}Ru_4Sn_{13-x}$
4	10	5	85	(1190, 900, 3)	15.2(2)	18.9(2)	65.9(2)	0.23(3)	9.7277(17)	$Ce_{3+x}Ru_4Sn_{13-x}$
5	13	5	82	(1200, 950, 1)	15.6(2)	18.9(2)	65.5(2)	0.34(3)	9.7272(16)	$Ce_{3+x}Ru_4Sn_{13-x}$
6	15	5	80	(1190, 900, 3)						$CeSn_3$
	La	Ru	Sn							
7	13	5	82	(1190,950,1)	16.7(0)	18.3(1)	65.1(1)	0.65(3)	9.7664(16)	$La_{3+x}Ru_4Sn_{13-x}$

[a]Initial loading composition.
[b]Temperature profile (maximum temperature, decanting temperature, and cooling rate in °C/hour).
[c]Composition obtained from EDX.
[d]Lattice parameter obtained from XRD.

The ampoules were heated and cooled in a furnace with the temperature profile in Table I. Right after the ampoules were removed from the furnace, the crystals were separated from the liquids with a centrifuge. The as-grown single crystals with dimensions of ~6 × 6 × 6 mm³ (~0.6 g) show clear faucets with Sn droplets on the surface, as shown in the inset of Fig. 1. The batch with 3% Ce (sample 0) yields only binary Ru_3Sn_7 and the batch with 15% Ce (sample 6) produces only $CeSn_3$. The decanting temperature of samples 1 and 5 was set to 950 °C to avoid Ru_3Sn_7 and $CeSn_3$ binary phases. It has to be noted that when the decanting temperature is set to 900 °C for the batch with 3.75% Ce (sample 1) both binary and ternary phases are obtained. However, raising the decanting temperature from 900 °C to 950 °C does not significantly affect the electrical resistivity (see results below). The single crystals of $La_{3+x}Ru_4Sn_{13-x}$ were prepared with the same growth condition as sample 5 in Table I.

The compositions of the grown single crystals were determined from energy-dispersive x-ray (EDX) spectra, obtained from a FEI Helios NanoLab 650 FIB/SEM system equipped with a EDAX Octane 60-mm² EDX detector. The EDX spectra were collected by selecting three 1500 μm × 500 μm areas with an accelerating voltage of 30 kV for 100 seconds. To verify the crystal structure of the title compound, powder x-ray diffraction (XRD) patterns of crushed single crystals were collected in a Rigaku MiniFlex diffractometer at room temperature. Silicon powders as an internal standard were added to correct the instrument's zero shift (Fig. 1). Large single crystals were cut into appropriate sizes using a wire saw and all surfaces were polished before performing physical property measurements. The DC magnetization, for temperatures ranging from 1.8 to 300 K and magnetic fields up to 70 kOe applied along the [100] crystallographic direction, was measured in a Quantum Design (QD) Magnetic Property Measurement System (MPMS). Electrical resistivity measurement was performed down to 1.8 K in a QD Physical Property Measurement Systems (PPMS). Specific heat was measured by the relaxation method down to $T = 0.4$ K for sample 5 and to $T = 1.8$ K for the rest of the samples in a QD PPMS.

III. RESULT AND DISCUSSION

Powder XRD patterns for sample 5, as representative data, are shown in Fig. 1. The observed peak positions are well indexed by the $Yb_3Rh_4Sn_{13}$-type structure ($Pm\bar{3}n$). Except for a low intensity Sn peak at around $2\theta \sim 30.5°$, no unindexed peaks or impurity phases are detected. It should be noted that the obtained XRD pattern can also be indexed with the $LaRuSn_3$-type structure ($Pm\bar{3}n$). The only difference between these two structure types is the Ce/Sn occupancy at the $2a$ site. Due to the subtle difference in their relative intensities, we were not able to distinguish between these two structure types. Therefore only the lattice parameter is obtained from the XRD patterns using the FULLPROF software [23].

The chemical compositions of the grown single crystals (samples 1–5), obtained from EDX analysis, are plotted in Fig. 2 as a function of initial Ce loading composition (Ce load percentage). The obtained Ce composition increases as Ce load percentage increases, whereas the Sn composition decreases as Ce load percentage increases. The composition of Ru remains relatively constant for all measured samples,
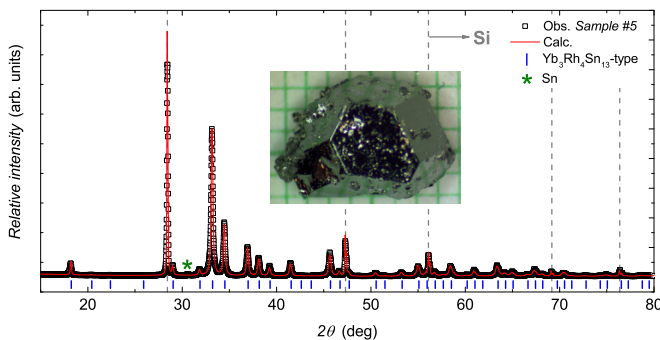

FIG. 1. Powder x-ray diffraction patterns of sample 5 together with Si powder. The black square symbols and red line denote the experimental data and calculated profiles, respectively. The vertical blue bars indicate the theoretical Bragg peak positions for the $Yb_3Rh_4Sn_{13}$-type structure. The Sn impurity phase is marked by the green asterisk. The vertical dashed lines represent the Si Bragg peak positions. Inset shows a photograph of sample 5 on a 1-mm grid.
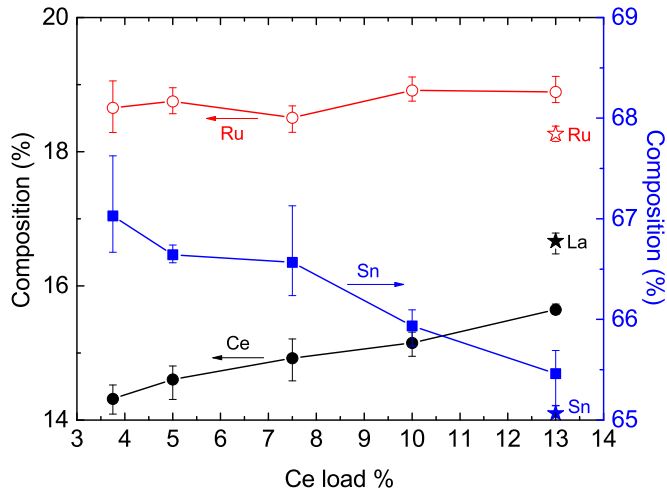
FIG. 2. Chemical compositions (%) of $Ce_{3+x}Ru_4Sn_{13-x}$ obtained from EDX, plotted as a function of Ce load percentage. The left and right axes represent the composition of Ce and Ru and the composition of Sn, respectively. EDX analysis of the La sample is presented by star symbols.

FIG. 3. Lattice parameter a, plotted as a function of x. Open symbols for $x = 0$ and 1 are taken from Refs. [24–26] and Refs. [10,19,20], respectively. Closed symbols for $0.05 < x < 0.34$ are obtained in this work.

suggesting the full occupancy of Ru at the $8e$ Wyckoff position. An earlier study on RPtIn$_3$ shows full occupancy at the $8e$, $6d$, and $24k$ sites and mixed occupancy at the $2a$ site [12]. This structural feature is prevalent in this family of materials, including $Ca_{3+x}Co_4Sn_{13-x}$ [11] and $Ce_{3+x}Ru_4Ge_{13-x}$ [13], as revealed by x-ray and neutron diffractions. In addition, the full occupancy of rare-earth atoms at the $2a$ site is realized in RRuSn$_3$ (R = La, Ce, Pr, and Nd) [10] and the full occupancy of Sn at the $2a$ site is revealed in $Ce_3Ru_4Sn_{13}$ [24]. Therefore we determined the chemical formula of the currently studied samples by fixing the averaged Ru composition of five samples to 4. When the mixed occupancy at the $2a$ site (Ce/Sn) and the full occupancy at the $8e$ (Ru), $6d$ (Ce), and $24k$ sites (Sn) are assumed, the obtained chemical formula are consistent with the general formula $Ce_{3+x}Ru_4Sn_{13-x}$. Based on this assumption we infer the Ce occupancy at the $2a$ site from x that is found to be 0.05 for the lowest Ce load percentage (sample 1) and 0.34 for the highest Ce load percentage (sample 5). Note that the EDX analysis does not provide the occupancy of atoms at their respective sites, and thus high-resolution x-ray experiments with Rietveld refinements must be performed to obtain the actual occupancies at given sites. The estimated x values are summarized in Table I, where x increases as Ce load percentage increases. The composition of the nonmagnetic analog is also obtained using the same EDX analysis and x value is found to be $x \simeq 0.65$.

The obtained lattice parameters are plotted in Fig. 3 as a function of x, together with earlier polycrystalline sample studies [10,19,20,24–26]. The x-error bars are based on the lower and upper bounds of averaged Ru composition and the y-error bars are estimated from the deviation of the expected Si Bragg peak positions. The lattice parameter obtained in this study generally decreases with increasing x, which is opposite to what has been reported in earlier studies. In the earlier polycrystalline sample studies, lattice parameters for all reported CeRuSn$_3$ samples ($x = 1$) [10,19,20] are larger
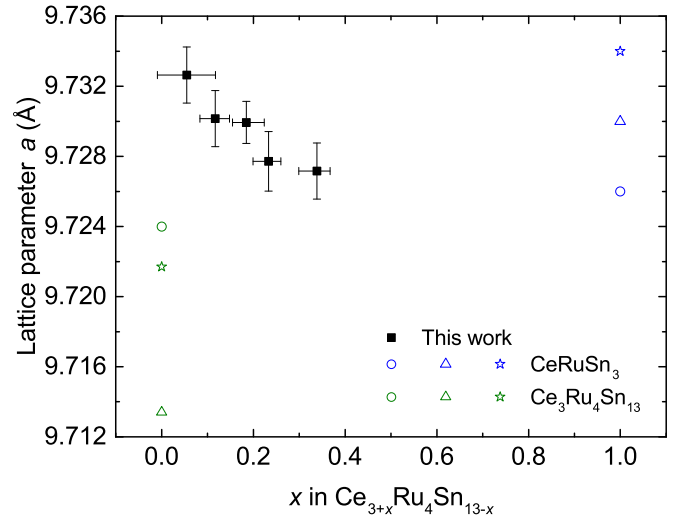
than that of all reported $Ce_3Ru_4Sn_{13}$ samples ($x = 0$) [24–26]. The XRD patterns of the compound $La_{3+x}Ru_4Sn_{13-x}$ can also be indexed with both the $Yb_3Rh_4Sn_{13}$-type and LaRuSn$_3$-type structures (not shown). The reported lattice parameter of $La_{3+x}Ru_4Sn_{13-x}$ compounds mostly ranges from $a = 9.766$ to 9.777 Å for $La_3Ru_4Sn_{13}$ [24,26] and from $a = 9.773$ to 9.782 Å for LaRuSn$_3$ [10,20,27]. The obtained lattice parameter $a = 9.7664(16)$ Å for $x = 0.65$ is slightly smaller than that for $x = 1$. The large fluctuation in the lattice parameter is probably due to the different sample quality and inconsistent method applied to obtain it. Thus the comparison of the lattice parameter is not conclusive and requires further investigation.

The observed physical properties of $La_{3.65}Ru_4Sn_{12.35}$ are consistent with a weakly diamagnetic intermetallic compound. The magnetization measurement at 1.8 K shows a very large diamagnetic signal below 5 kOe due to the superconducting phase and shows an increase in negative magnetization at high magnetic fields, as shown in Fig. 4(a). The magnetic susceptibility, $M(T)/H$, at 70 kOe (left inset) weakly depends on temperature with a very small average value. In the zero-field-cooled measurement at 1 kOe, the superconducting transition occurs at about 2 K (right inset). Since the flat region of the superconducting state does not appear in the magnetic susceptibility, the concentration of the superconducting phase is not possible to estimate. Figure 4(b) shows the electrical resistivity, $\rho(T)$, of $La_{3.65}Ru_4Sn_{12.35}$. $\rho(T)$ follows metallic behavior (e.g., $d\rho/dT > 0$) at high temperatures and indicates a superconducting transition at $T_{SC} = 2.1$ K (inset). Although the observed metallic behavior is consistent with an earlier polycrystalline $La_3Ru_4Sn_{13}$ sample [18], the absolute value of the resistivity is roughly four times smaller than that of the polycrystalline sample. In addition, T_{SC} of the single crystal is slightly higher than the reported transition temperature of $\sim$1.5 K [18]. The difference could be due to the sample quality. Note that semiconductorlike behavior is observed for the polycrystalline LaRuSn$_3$ sample [28].
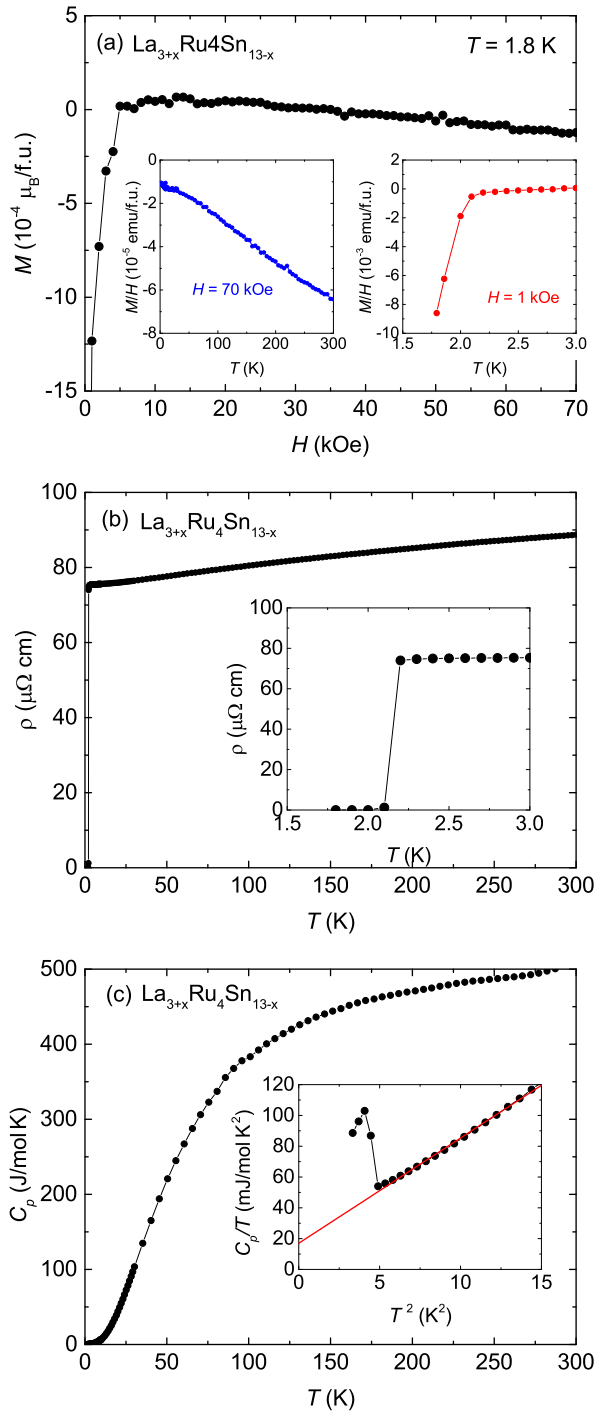
FIG. 4. Physical properties of La$_{3+x}$Ru$_4$Sn$_{13-x}$ for $x = 0.65$. (a) $M(H)$ for $H \parallel$ [100] at $T = 1.8$ K. Insets show M/H at $H = 70$ kOe (left) below 300 K and at 1 kOe below 3 K (right). (b) $\rho(T)$ below 300 K. Inset shows the expanded plot below 3 K. (c) C_p per formula unit. Inset shows C/T vs T^2 plot. Solid line represents the fit to $\gamma T + \beta T^3$.

The specific heat, C_p, of La$_{3.65}$Ru$_4$Sn$_{12.35}$ as a function of temperature is shown in Fig. 4(c). The C_p measurement clearly confirms the superconducting phase transition at $T \sim 2.1$ K, as shown in the inset, where the peak position of the maximum coincides with the resistivity signature. Since the resistivity
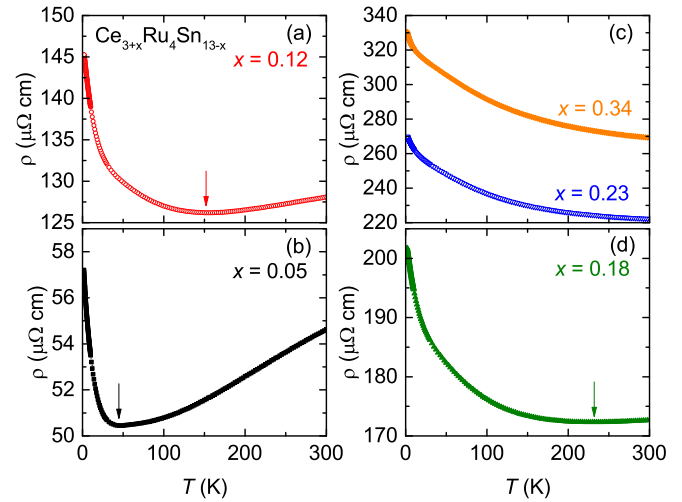

FIG. 5. $\rho(T)$ of Ce$_{3+x}$Ru$_4$Sn$_{13-x}$ for (a) $x = 0.12$, (b) 0.05, (c) 0.23 and 0.34, and (d) 0.18. Vertical arrows indicate the position of the resistivity minimum $T_{\min}$.

value goes to zero in the superconducting state and the specific heat shows a jump at $\sim$2.1 K, the bulk superconducting phase transition is the ternary phase, not from an impurity or Sn phase. Above T_{SC} the electronic and phonon contributions are estimated by $C_p = \gamma T + \beta T^3$. The electronic contribution γ and Debye temperature Θ_D are obtained to be $\sim$16.95 mJ mol^{-1} K^{-2} and $\sim$170 K, respectively, from the C_p/T versus T^2 plot (inset). The obtained Debye temperature is consistent with the earlier study ($\Theta_D = 150$ K [18]). By using the obtained γ value, the specific heat jump $\Delta C_p/(\gamma T_{SC}) = 1.46$ is found to be only slightly above 1.43, indicating that the superconductivity in the La$_{3.65}$Ru$_4$Sn$_{12.35}$ compound can be ascribed to the conventional isotropic BCS type.

The $\rho(T)$ curves of Ce$_{3+x}$Ru$_4$Sn$_{13-x}$ for samples 1–5 (0.05 $\leqslant x \leqslant$ 0.34) are shown in Fig. 5. The absolute value of the electrical resistivity for the entire temperature range measured increases as x increases. For $x = 0.05$ [Fig. 5(b)], $\rho(T)$ follows Kondo lattice behavior with a resistivity minimum at $T_{\min} \sim 45$ K. $T_{\min}$ gradually moves to higher temperature as x increases. For $x \geqslant 0.23$, the resistivity, upon cooling, continuously increases without the minimum. The evolution of $\rho(T)$ as a function of x can be seen better from the resistivity curves normalized at 300 K. To compare, the normalized resistivity curves of polycrystalline Ce$_3$Ru$_4$Sn$_{13}$ ($x = 0$) [18] and CeRuSn$_3$ ($x = 1$) [22] are plotted together with the currently studied single crystals in Fig. 6. The normalized $\rho(T)$ curves of Ce$_{3+x}$Ru$_4$Sn$_{13-x}$ single crystals systematically vary between $x = 0$ and $x = 1$. The resistivity value at 300 K, $\rho(T = 300$ K), and the observed $T_{\min}$ for various x are plotted in Fig. 7, where both $\rho(T = 300$ K) and $T_{\min}$ increase quasi-linearly as x increases. It should be noted that $\rho(T = 300$ K) for polycrystalline Ce$_3$Ru$_4$Sn$_{13}$ is much higher than that for samples with $x > 0$.

$\rho(T)$ of the Ce$_{3+x}$Ru$_4$Sn$_{13-x}$ system is very sensitive to the initial stoichiometric ratios of the constituent elements. In addition, the cooling rates and decanting temperatures of the samples appear to be critical parameters for the absolute value of the electrical resistivity. We have grown multiple
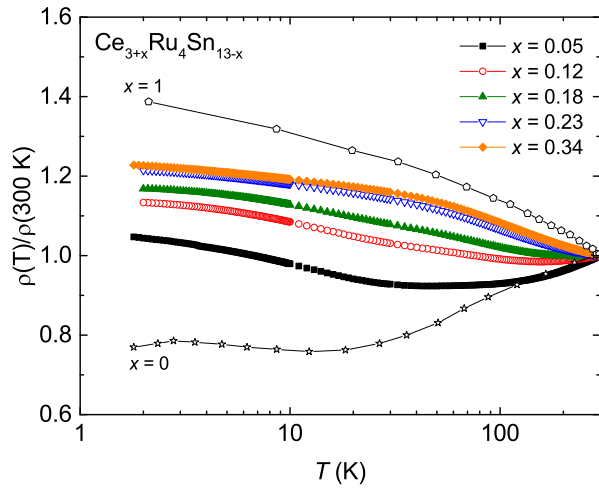
FIG. 6. Normalized electrical resistivity, $\rho(T)/\rho(300\,\text{K})$, curves for various x. Data for Ce$_3$Ru$_4$Sn$_{13}$ ($x = 0$) [18] and CeRuSn$_3$ ($x = 1$) [22] are taken by hand from the references and normalized at 300 K.

samples for $x = 0.05$ with different cooling rates (1–10 °C per hour) and slightly different decanting temperatures. Figure 8 shows the normalized resistivity curves of sample 1, a sample with a 900 °C decanting temperature and cooling rate of 1 °C/h (sample D900), and a sample with a 950 °C decanting temperature and cooling rate of 10 °C/h (sample C10). The normalized resistivity curves of the three samples are almost identical, with the temperature dependencies and $T_{\min}$ remaining the same. However, the absolute value of the resistivity is affected by the temperature profiles, as shown in the inset of Fig. 8, which is probably driven by the large degree of grain boundary effects.

With varying the occupancy of Ce at the $2a$ site, the electrical resistivity of the Ce$_{3+x}$Ru$_4$Sn$_{13-x}$ system drastically changes from metallic Kondo lattice behavior ($x = 0$)
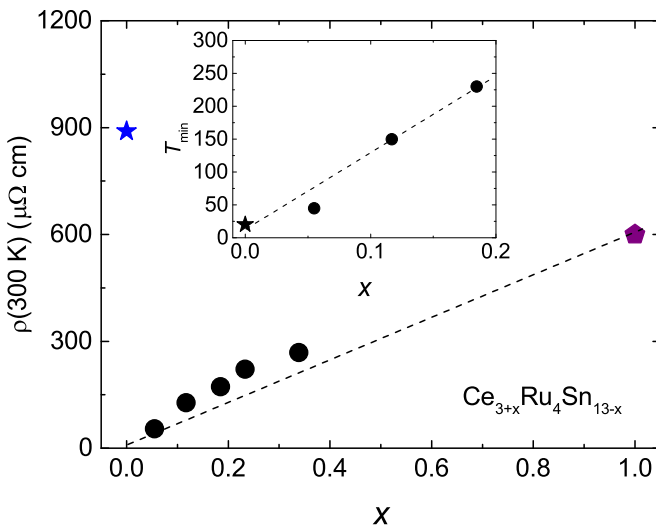

FIG. 7. Resistivity value at 300 K, $\rho(300\,\text{K})$, for various x. Inset shows the resistivity minimum, $T_{\min}$, for $x < 0.2$. Star ($x = 0$) and pentagon ($x = 1$) symbols are taken from Refs. [18,22], respectively. Lines are guides to the eyes.
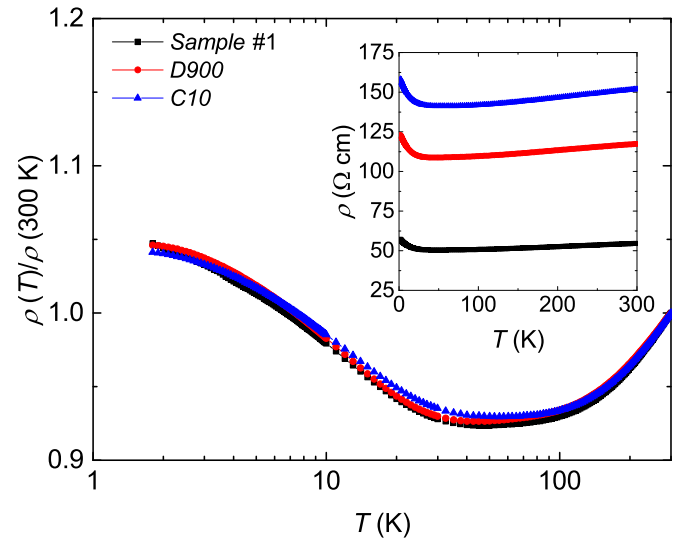

FIG. 8. $\rho(T)/\rho(300\,\text{K})$ curves of samples 1, D900, and C10. (See the main text for details). Inset shows $\rho(T)$ of samples 1, D900, and C10.

to semiconductorlike behavior below 300 K ($x = 1$). Such sample-dependent electrical resistivity has been observed in earlier polycrystalline CeRuSn$_x$ ($2.85 \leqslant x \leqslant 3.15$) samples [29], where the absolute value of the resistivity becomes smaller when varying x from 3, and drastic changes in $\rho(T)$ are observed at low temperatures for both the Sn-excess case ($x > 3$) and Sn-deficient case ($x < 3$). Since the $2a$ site in Ce$_{3+x}$Ru$_4$Sn$_{13-x}$ is occupied by both Ce and Sn atoms, the systematic variation of the electrical resistivity can be related to the site disorder. It has been empirically demonstrated that a semiconductorlike enhancement of resistivity upon cooling in germanides with Yb$_3$Rh$_4$Sn$_{13}$-type structures is related to the large crystallographic disorder: the ratio of the atomic displacement parameter (ADP) between the $2a$ site atom and transition metal atom correlates well to the resistivity data [3]. Note that the ADP ratio of 3-4-13 germanides is generally greater than that for metallic stannides [3]. In the currently studied samples, the highest disorder is expected from La$_{3+x}$Ru$_4$Sn$_{13-x}$ with $x = 0.65$, however the resistivity shows metallic behavior. It is expected from the inset of Fig. 7 that the $T_{\min}$ value for $x > 0.18$ is higher than 300 K. Therefore it is not unreasonable to assume that the semiconductorlike behavior ($d\rho(T)/dT < 0$) observed for $x > 0.18$ originates from Kondo scattering below $T_{\min}$.

In the current study, the importance of Kondo scattering in conjunction with the crystalline electric field (CEF) effect complicates a straightforward interpretation of the resistivity data. In zero field, the combined Kondo and RKKY interactions qualitatively explain the resistivity of various Kondo lattice systems. Since no magnetic ordering has been observed in Ce$_{3+x}$Ru$_4$Sn$_{13-x}$ ($0 \leqslant x \leqslant 1$) compounds, the Kondo interaction overcomes the RKKY exchange interaction and thus a normal Fermi liquid should be realized in this system. The single-impurity Kondo-like resistivity in all samples at low temperatures and the absence of a T^2 Fermi liquid regime below the coherence temperature are puzzling. Therefore the resistivity is measured under external magnetic fields that
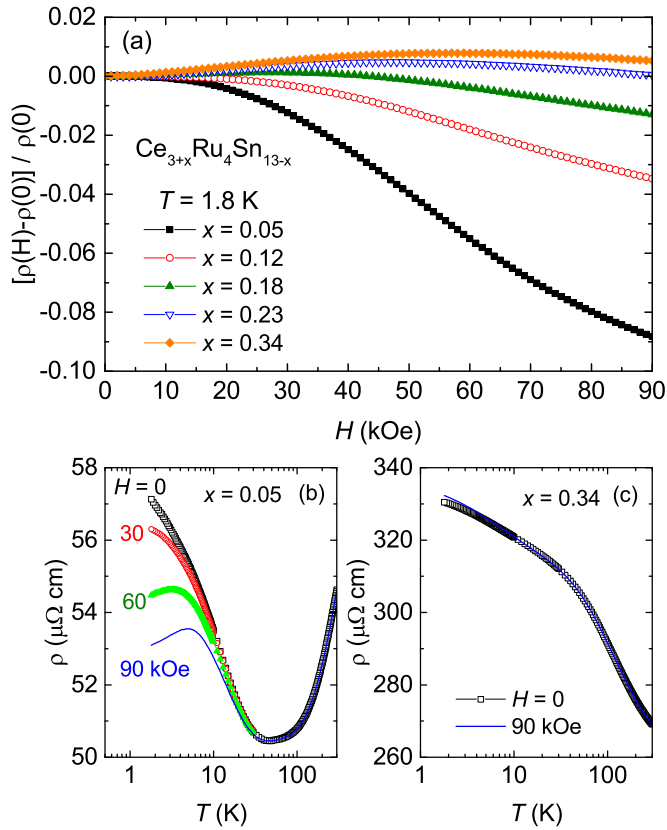
FIG. 9. (a) Magnetoresistance, $[\rho(H) - \rho(0)]/\rho(0)$, at $T = 1.8$ K for various x. (b) $\rho(T)$ of $x = 0.05$ at $H = 0, 30, 60$, and 90 kOe. (c) $\rho(T)$ of $x = 0.34$ at $H = 0$ and 90 kOe.

will suppress the contributions of both Kondo and RKKY scattering at different rates. The magnetoresistance (MR) of $Ce_{3+x}Ru_4Sn_{13-x}$ at 1.8 K for $H \parallel [100]$ is shown in Fig. 9(a). Although the relative variation of MR is small for all x, probably due to the disorder, the MR curves clearly show a systematic evolution, changing from negative to positive MR as x increases. MR for $x = 0.05$ is negative for all measured fields, suggesting that the $\rho(T)$ upturn below T_{min} could arise due to the Kondo interaction.

The $\rho(T)$ curves at various magnetic fields further support the Kondo effect. In zero field, a logarithmic increase of the resistivity with decreasing temperature, $\rho(T) \sim -\log(T)$, indicates incoherent Kondo scattering as shown in Fig. 9(b). At low temperatures, a magnetic field suppresses spin-flip scattering, causing the negative MR and the development of a maximum (coherence). The maximum moves to a higher temperature as magnetic field increases, which is consistent with the behavior observed in many heavy fermion (Kondo lattice) systems. The MR curve for $x = 0.34$ is positive at low fields but starts showing a negative trend as the field increases further. In zero field, $\rho(T) \propto -\log(T)$ behavior is dominant, however the resistivity measurements indicate a negligible MR as shown in Fig. 9(c). It will require a much higher magnetic field to observe the maximum in the resistivity. We conjecture that the evolution of MR as a function of x is caused by the combination of Kondo scattering at the $6d$ site and an increase in the randomness of f-electron scattering at the $2a$

site. It should be distinguished from the effect of dilution of f sites (i.e., the Ce-ions are replaced by non-f ions like La ions). It has been shown that different Kondo systems exhibit positive or negative MR depending on the temperature regime, the number of occupied f electrons per site, and the Kondo temperature. For the $Ce_{3+x}Ru_4Sn_{13-x}$ system, the disorder (especially related to the $2a$ site) increases as x increases, implying that the random f-electron scatterings become significant for higher x. We note that the enhancement of RKKY scattering for higher x may provide an alternate explanation of the positive MR contributions. Our results suggest the relative importance of disorder contributions that may have a strong influence on the electrical resistivity.

Inverse magnetic susceptibility, $1/\chi(T) = H/M$, curves for $Ce_{3+x}Ru_4Sn_{13-x}$ single crystals are shown in Fig. 10(a). All curves show a slight deviation from the linear temperature dependence above $\sim$150 K. Therefore the effective moments, μ_{eff}, and Weiss temperatures, θ_p, are estimated by fitting $1/\chi(T)$ curves to modified Curie-Weiss (C-W) law: $\chi(T) = \chi_0 + C/(T - \theta_p)$. The obtained results are plotted in Fig. 10(b) together with values from the previous polycrystalline sample studies [20,22,24]. The μ_{eff} values of single-crystal samples are close to the expected free Ce^{3+}-ion value (2.54 μ_B). Note that μ_{eff} values for polycrystalline samples are slightly smaller than the theoretical value. The estimated θ_p values ($\sim$$-40$ K) for single-crystal samples are almost independent of x, but larger than those for polycrystalline $CeRuSn_3$ and $Ce_3Ru_4Sn_{13}$ samples. It has to be noted that the obtained paramagnetic χ_0 values are in the range of $\sim 1 \times 10^{-4}$ emu/f.u., which is somewhat bigger than the diamagnetic response of La-compound, plotted in the inset of Fig. 4(a). It is interesting to note that mixed valence behavior has been previously observed in 3-4-13 germanides $Ce_3Ru_4Ge_{13}$, $Ce_3Os_4Ge_{13}$, and $Ce_3Ir_4Ge_{13}$ [13,30,31]. Both μ_{eff} and θ_p values in $Ce_{3+x}Ru_4Sn_{13-x}$ show no correlation with x, suggesting that Ce-ions in these compounds retain the 3+ valence state at both the $6d$ and $2a$ sites. This result is consistent with the absence of the f^0 peak associated with tetravalent Ce-ions in core-level photoemission spectra in polycrystalline $CeRuSn_3$ and $Ce_3Ru_4Sn_{13}$ samples [26,32].

Figure 10(c) shows magnetic susceptibility, M/H, curves for $Ce_{3+x}Ru_4Sn_{13-x}$ single crystals. Unlike the high temperature magnetic response, the low temperature M/H curves exhibit strong x dependence. The M/H curve for $x = 0.34$ continuously increases with decreasing temperature, whereas a clear broad maximum is detected at $\sim$3.5 K for the $x = 0.05$ sample. The observed maximum gradually disappears with increasing x. It has been shown that peaks are found in the magnetic susceptibility for $J > 3/2$ [degeneracy $N = (2J + 1) > 2$] and that these peaks become pronounced as the degeneracy increases [33]. Such peaks have been observed for many Ce ($J = 5/2$) and Yb ($J = 7/2$) based Kondo lattice compounds [34–40]. Note that a similar broad maximum in the magnetic susceptibility is also observed at a much lower temperature $T \sim 0.6$ K in a $CeRuSn_3$ polycrystalline sample [22], but no maximum is observed down to 1.8 K in a $Ce_3Ru_4Sn_{13}$ polycrystalline sample [18]. μSR and inelastic neutron scattering studies on the $CeRuSn_3$ compound suggest that the broad maximum at $T \sim 0.6$ K observed in specific heat and magnetic susceptibility is re-
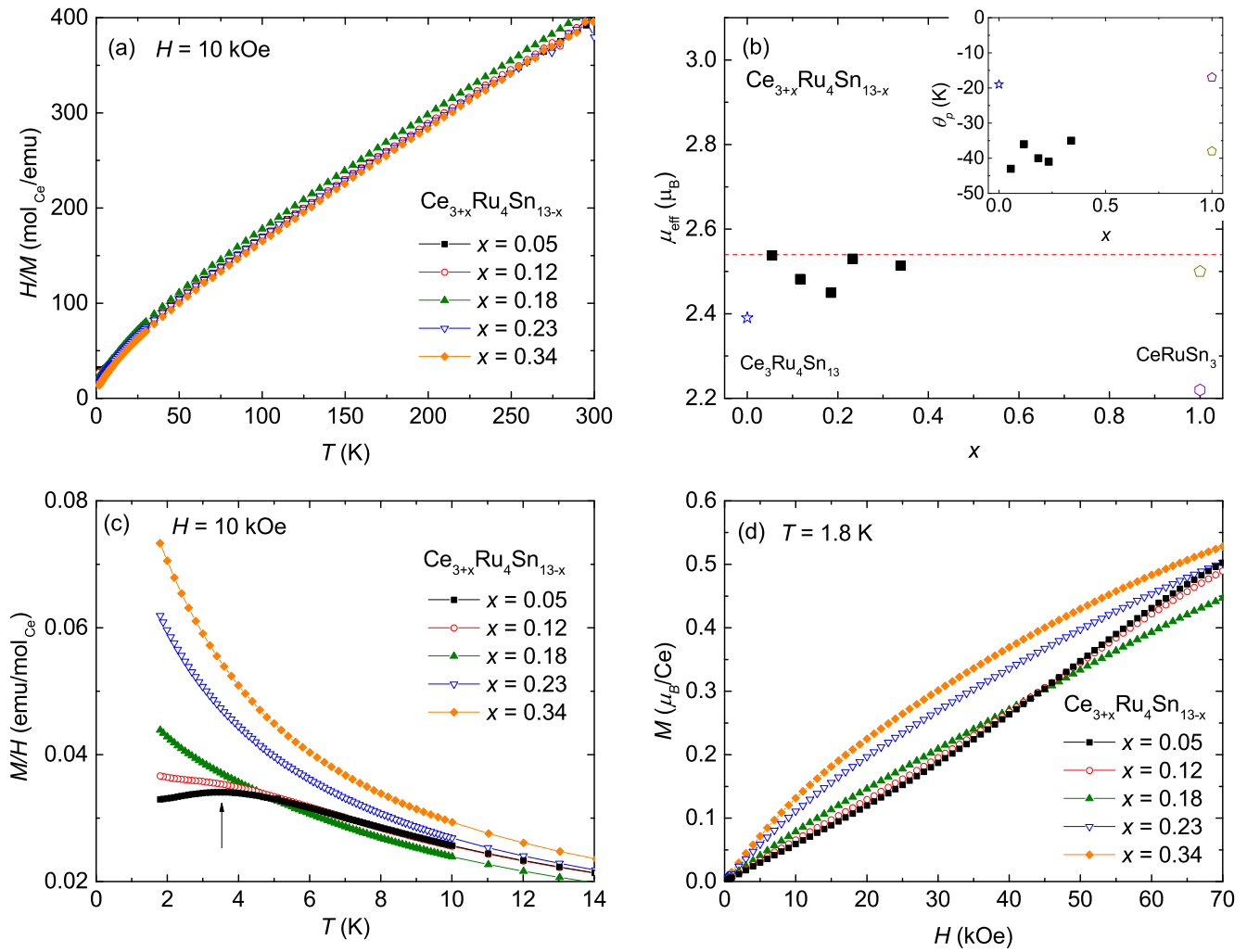
FIG. 10. (a) Inverse magnetic susceptibility, H/M, of $Ce_{3+x}Ru_4Sn_{13-x}$ single crystals at $H = 10$ kOe along $H \parallel [100]$. (b) Effective moment μ_{eff} and Weiss temperature θ_p (inset) as a function of x. Open symbols are taken from previous studies of polycrystalline $Ce_3Ru_4Sn_{13}$ [24] and $CeRuSn_3$ [20,22]. The dotted line is the theoretical value of the effective moment for the free Ce^{3+}-ion. (c) Magnetic susceptibility, M/H, of $Ce_{3+x}Ru_4Sn_{13-x}$ single crystals below 14 K. Vertical arrow indicates a broad maximum at ~ 3.5 K for $x = 0.05$. (d) Magnetization isotherms at 1.8 K along $H \parallel [100]$.

lated to either short-range magnetic fluctuations or spin-glass dynamics [19,22].

The magnetization isotherms, $M(H)$, at $T = 1.8$ K for various x are plotted in Fig. 10(d). The $M(H)$ curves for $x = 0.34$ and 0.23 follow Brillouin functionlike behavior, whereas the curves with lower x show an increasing slope up to ~ 50 kOe. The magnetization value at 70 kOe for all x reaches ~ 0.5 μ_B/Ce, which is much smaller than the saturated magnetization value of the free Ce^{3+}-ion (2.14 μ_B/Ce). This reduced magnetization value could be due to the Kondo effect in conjunction with the CEF effect. Since the magnetic susceptibility measurements for $Ce_{3+x}Ru_4Sn_{13-x}$ single crystals indicate no magnetic ordering down to 1.8 K, the slope change clearly observed in $M(H)$ for $x = 0.05$ cannot be related to a metamagnetic transition generally shown in antiferromagnets. We note that an abrupt nonlinear increase of magnetization has been observed in the heavy fermion metamagnet $CeRu_2Si_2$ [41].

Specific heat curves divided by temperature, C_p/T, for $Ce_{3+x}Ru_4Sn_{13-x}$ single crystals are plotted in Fig. 11(a). The curves display a minimum at ~ 8 K with $C_p/T \sim 1$ J mol$_{Ce}^{-1}$ K^{-2}, and show large enhancement below this minimum. The specific heat, C_p, curves below 10 K are shown in the inset of Fig. 11(a). A broad hump below 8 K is observed for all x, which corresponds to the enhancement of C_p/T. For $x = 0.05$, the observed C_p/T down to 1.8 K is consistent with the earlier polycrystalline $Ce_3Ru_4Sn_{13}$ sample [18]. For $x = 0.34$, a broad maximum with $C_p/T \sim 4$ J/mole-K^2 is detected around 0.5 K, which coincides with a maximum observed from the specific heat measurement of a polycrystalline $CeRuSn_3$ sample [21]. C_p/T of $La_{3.65}Ru_4Sn_{12.35}$ is comparable to that of $Ce_{3+x}Ru_4Sn_{13-x}$ above 100 K, whereas the difference between the La- and Ce-based compounds becomes significant below the minimum. Therefore the upturn below the minimum suggests significant magnetic contributions.
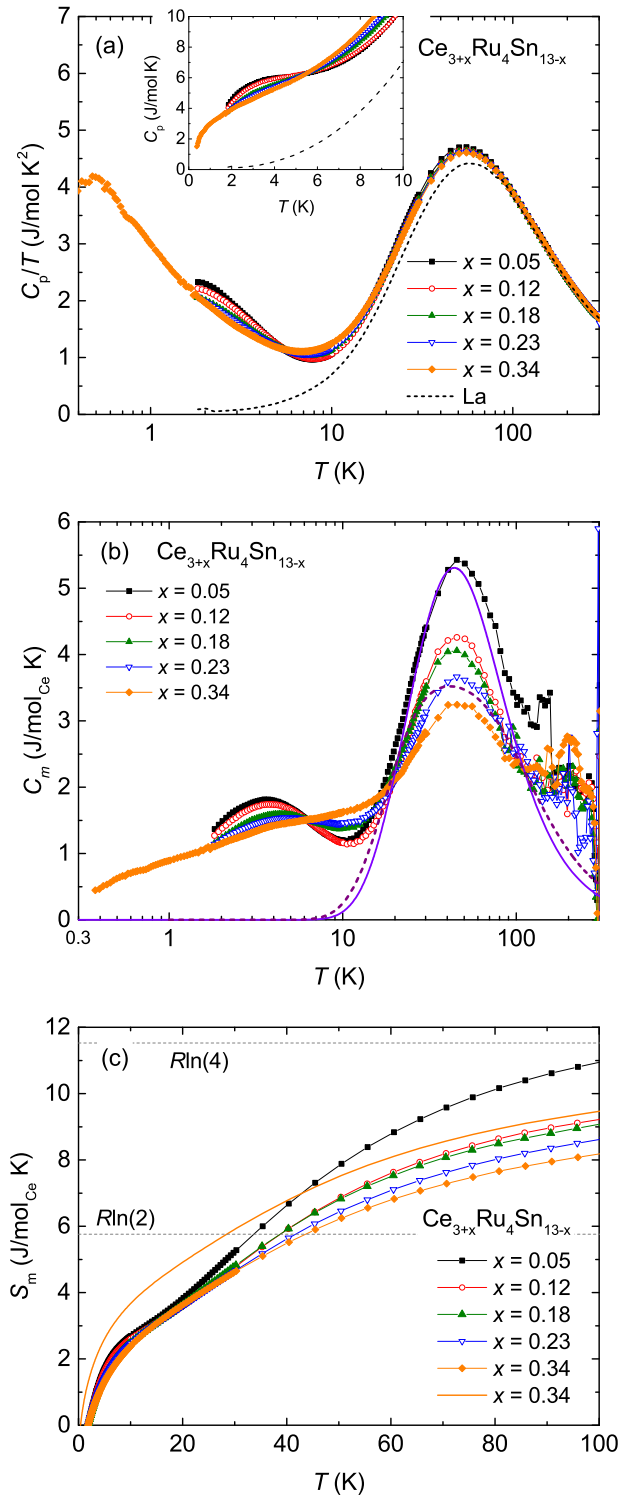
FIG. 11. (a) C_p/T vs T plots for $Ce_{3+x}Ru_4Sn_{13-x}$ (symbols) and $La_{3+x}Ru_4Sn_{13-x}$ (dashed line). Inset shows C_p vs T below 10 K. (b) C_m for $Ce_{3+x}Ru_4Sn_{13-x}$. The solid line is the Schottky calculation with $\Delta_1 = 85$ K and $\Delta_2 = 165$ K. The dashed line represents the CEF contributions based on Ref. [19]. (c) Magnetic entropy S_m for $Ce_{3+x}Ru_4Sn_{13-x}$. The solid line is the magnetic entropy obtained by integrating C_m/T from 0.4 K for $x = 0.34$.

The nature of the magnetic state of $Ce_{3+x}Ru_4Sn_{13-x}$ can be inferred by examining the magnetic contribution to the specific heat C_m. The C_m curves with various x are plotted in Fig. 11(b), where C_m is estimated by subtracting the specific heat of the nonmagnetic analog $La_{3.65}Ru_4Sn_{12.35}$. For $x = 0.05$, the C_m curve clearly shows two broad maxima at ~3.5 and ~50 K. With increasing x the absolute value of C_m becomes smaller for both maxima, while the broad peak on the high temperature side remains at almost the same temperature. For $x = 0.34$, C_m indicates no clear maximum in the low temperature regime. The electronic contribution to the specific heat is difficult to determine because C_m/T does not saturate below 8 K. We note that a large C/T value at low temperatures has been reported for the isostructural $Ce_{3+x}Ru_4Sn_{13-x}$ family and other compounds with the $Yb_3Rh_4Ge_{13}$-type structure [7,13,18,21,22,42].

The magnetic entropy S_m of $Ce_{3+x}Ru_4Sn_{13-x}$ is estimated by integrating C_m/T, and is plotted in Fig. 11(c). Because of the upturn in C_m/T below 10 K, the extrapolation of the specific heat to $T = 0$ cannot be made without ambiguity. Thus, to compare the evolution of S_m as a function of x, the integration of C_m/T has been performed from 1.8 K for all x. For $x = 0.34$, the specific heat is measured from 0.4 K, and thus the entropy is also estimated by integrating C_m/T from 0.4 K and is plotted in the same figure with a solid line. As is clear from the case $x = 0.34$, the total S_m is underestimated by at least ~1 J mol$_{Ce}^{-1}$ K^{-1}. For $x = 0.05$, S_m reaches $R\ln(4)$ around 100 K, indicating that there are two doublets mainly influencing C_m, with the third doublet outside of this temperature window. Although the missing entropy below 1.8 K has to be considered, the magnetic entropy approaches $R\ln(2)$ around 30–40 K for all x, suggesting that the low temperature maximum is mostly associated with either the ground state doublet or the combination of a doublet and quartet with small CEF splittings. The remaining entropy is removed far above this temperature.

The high-temperature broad peak can be attributed to the Schottky anomaly. Such a maximum is typically shown in magnetic specific heat due to the splitting of the six-fold degenerate multiplet in Ce^{3+} ions. For the $x = 0$ case ($Ce_3Ru_4Sn_{13}$), the Ce^{3+}-ions occupy only the $6d$ site, and thus the tetragonal point symmetry at the Ce site splits the $J = 5/2$ Hund's rule multiplet of the Ce^{3+} ions into three doublets. For $Ce_{3+x}Ru_4Sn_{13-x}$ systems the analysis of the Schottky anomaly becomes more complex, as the actual occupancy of Ce-ions at both the $6d$ and $2a$ (cubic point symmetry) sites must be considered to properly account for CEF effects. In the present study ($0.05 < x < 0.34$) the variation in C_m curves between samples with lowest x and highest x is about ~2 J mol$_{Ce}^{-1}$ K^{-1}, which is comparable to the uncertainty in C_m estimation. The absolute value of C_m for $Ce_{3+x}Ru_4Sn_{13-x}$ compounds is dependent on the actual Ce concentrations, and is also largely affected by the subtraction of the nonmagnetic analog La compound. Due to these uncertainties the absolute value of C_m can vary by as much as 1.4 J mol$_{Ce}^{-1}$ K^{-1}. In particular, difficulty in accurately modeling the nonmagnetic contribution with $La_{3+x}Ru_4Sn_{13-x}$

at high temperatures prevents us from doing quantitative analysis of Schottky contributions as suggested in Ref. [19]. The Schottky contributions in CeRuSn$_3$, combined with inelastic neutron scattering data, are reproduced by considering a 25% contribution from cubic symmetry and 75% from tetragonal symmetry: the Ce ions at the 2a site have a quartet as a ground state and a doublet as an excited state with an energy gap $\Delta \sim$ 95 K, and the Ce ions at the 6d site have three doublets with energy gaps $\Delta_1 \sim 72$ K and $\Delta_2 \sim 223$ K [19].

For $x = 0.05$, it is reasonable to assume that cubic CEF effects are negligible, and thus the C_m curve can be analyzed by considering Ce ions at only the 6d site. The Schottky contribution is denoted by a solid line in Fig. 11(b), involving three doublets separated by $\Delta_1 = 85$ K and $\Delta_2 = 165$ K. It is clear from the figure that the position of the broad maximum can be reproduced by the Schottky calculation. We expect that the difference between C_m and the Schottky calculation is probably due to subtraction error. The Schottky contribution based on Ref. [19] (dashed line) is also plotted in the same figure, accounting for CEF contributions from both the 2a and 6d sites. For $x > 0.05$, the position of the broad maximum at ~ 50 K and the decrease in the absolute value of the C_m curves can be qualitatively explained by considering CEF contributions according to the multiplicities of both Ce-site point symmetries. It has to be noted for cubic symmetry sites that the systematic change in C_m while varying x cannot be reproduced by considering the doublet ground state. To perform more quantitative analysis, it is necessary to have more reliable composition analysis to obtain actual Ce-ion occupancies between the 6d and 2a sites and subtract the nonmagnetic contributions accurately.

At low temperatures, because the absolute value of C_m is not sensitive to subtracting the specific heat of La-based compound, it is reasonable to assume that C_m solely consists of Ce-ions' magnetic contributions. For $x = 0.05$, the broad peak in C_m at ~ 3.5 K may have the same origin as the broad peak observed in the magnetic susceptibility, which is reminiscent of the Kondo effect with degenerate ground states. With increasing x, the height of the broad peak decreases and the peak becomes broader. The specific heat measurement of a previous polycrystalline Ce$_3$Ru$_4$Sn$_{13}$ sample shows a broad peak around ~ 3 K, where a very large enhancement of C/T below 8 K accompanied with a broad feature around 2 K is explained by considering two low lying CEF doublets with $\Delta = 8$ K and the Kondo effect with $T_K = 2$ K [18]. Note that the absolute value of the specific heat of Ce$_3$Ru$_4$Sn$_{13}$ [18] is roughly twice bigger than that of $x = 0.05$. In the present study, both the width and height of the broad peak for all x cannot be reproduced by the Schottky anomaly, ruling out low lying CEF doublets as its origin. In addition, the entropy recovering $R \ln(2)$ at ~ 30 K is inconsistent with two low lying CEF doublets with a small splitting.

For Ce- and Yb-based Kondo lattice compounds, the Kondo temperature T_K and the ground state degeneracy play important roles in the thermodynamic and transport properties [43]. The peak observed in $\chi(T)$ and $C_m(T)$ may be a result of the orbital effect of total angular momentum J larger than 1/2, as proposed by Coqblin and Schrieffer (C-S) [44]. In this model the multiplicity $N = 2J + 1$ of the total angular momentum plays an important role in stabilizing the Kondo state
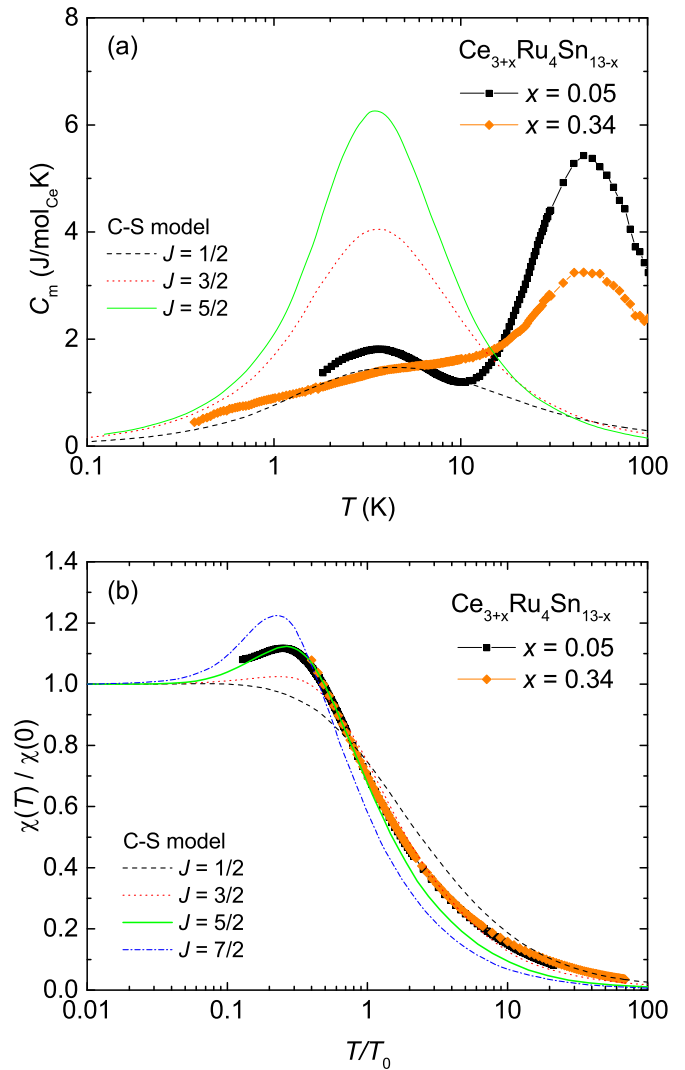

FIG. 12. (a) C_m for $x = 0.05$ and 0.34. Lines represent the prediction of the Coqblin-Schrieffer model for $J = 1/2$, 3/2, and 5/2 and $T_0 = 5$, 8, and 12 K, respectively. (b) $\chi(T)/\chi(0)$ for $x = 0.05$ and 0.34. Lines represent the prediction of the Coqblin-Schrieffer model for $J = 1/2$, 3/2, 5/2, and 7/2.

and raising the Kondo temperature T_K. The Kondo impurity problem in the Coqblin-Schrieffer model has been numerically calculated for several total angular momenta by Rajan [33]. Generally specific heat and magnetic susceptibility show a the maximum for $N > 2$ and the temperature of the maximum is related to T_K [33]. The low-temperature C_m curves for $x = 0.05$ and 0.34 are compared with Rajan's calculations as shown in Fig. 12(a). The maximum in C_m for $x = 0.05$ falls between the $J = 1/2$ and 3/2 curves, indicating that the Kondo effect combined with CEF splitting scheme will not allow this very simple type of analysis. By considering the entropy and the large C_m/T value at low temperatures it is expected that $T_K < \Delta$ for all x, where Δ is the energy gap between the ground and first excited states of CEF levels. Based on this, for $x = 0.05$, it is reasonable to assume that the maximum in C_m simply reflects the Kondo effect, with the doubly degenerate case corresponding to $N = 2$. For $x = 0.34$, the

two extrema in the specific heat data associated with Kondo effects on the CEF ground states of both the $6d$ and $2a$ sites could be expected. However, only one broad peak structure is developed. We thus expect that a single broad maximum is produced by merging more than one peak structure associated with different Kondo temperatures for the $2a$ and $6d$ sites. A similar analysis can be made by performing a fit to the magnetic susceptibility over a wide temperature range. As shown in Fig. 12(b) the magnetic susceptibility curves for both $x = 0.05$ and 0.34 cannot be explained by the C-S model with any J value over the entire temperature range measured. Therefore we compare the height of the maximum with the C-S model. When the magnetic susceptibility for $x = 0.05$ is scaled with $\chi_0 = 0.031$ emu/mole and $T_0 = 14$ K, the broad maximum can be described by the $J = 5/2$ case, implying that the state with $N = 6$ is Kondo screened and $T_K > \Delta$. However, in the high temperature regime, the susceptibility curve follows the C-S model with $J = 3/2$. This is in contrast with the magnetic specific heat analysis. Interestingly, when the susceptibility curve for $x = 0.34$ is scaled with $\chi_0 = 0.068$ emu/mole and $T_0 = 4.5$ K, it follows the $\chi(T)$ curve of $x = 0.05$, implying that there might be a maximum below 1.8 K in $\chi(T)$ for $x = 0.34$. Given the above analysis, the CEF splitting scheme with doublet and quartet ground states will not allow this very simple type of analysis with the Kondo interaction. It has to be noted that the maximum in $\chi(T)$ and the metamagnetic-like transition can be developed with Kramers doublet ($N = 2$) as evidenced from CeRu$_2$Si$_2$ [41], where the anisotropic hybridization is suggested to be the origin [45,46]. Further studies are necessary to understand the origin of the maximum in $\chi(T)$ and the metamagnetic-like transition in $M(H)$ for $x = 0.05$.

The electrical resistivity, specific heat, and magnetic susceptibility data suggest that Ce$_{3+x}$Ru$_4$Sn$_{13-x}$ compounds are heavy fermion Kondo lattice systems with complex CEF schemes. However, it shouldn't be discarded the possibilities that the low temperature physical properties result from magnetic fluctuations, disorder, or spin glass. Neutron scattering and μSR studies on CeRuSn$_3$ suggest that the low temperature broad peak is related to short-range magnetic fluctuations or spin-glass dynamics [19,22]. Although no hysteresis is observed for all samples in this study, the low temperature specific heat and magnetic susceptibility may result from the spin glass. The key ingredients for spin glass behavior are frustration and disorder (randomness). When Ce atoms at $6d$ site are considered, the Ce sublattice forms icosahedra, but distorted. Within each icosahedron, the Ce atoms are located on isosceles triangles with a distance $\sim$4.86 Å from the nearest Ce atoms and $\sim$5.95 Å from the next nearest Ce atoms. When three Ce spins are placed on isosceles triangle (not placed on equilateral triangle), the frustration is not expected in this system. Therefore the spin glass behavior observed in earlier studies might be caused by the disorder.

With regard to the disorder, the formation of superstructure mostly related to the distorted icosahedra in the Yb$_3$Rh$_4$Sn$_{13}$-type structure is evidenced [47] and the Ce occupancies at both the $6d$ and $2a$ sites are critical to interpret the physical properties on Ce$_{3+x}$Ru$_4$Sn$_{13-x}$ system [22]. In addition, the electrical resistivity of Ce$_3$Co$_4$Sn$_{13}$ [42] and Ce$_3$Rh$_4$Sn$_{13}$ [48] show anomalous behavior below the structural phase transition which is due to a small distortion of trigonal Sn prisms around transition metal ions. Interestingly, the Weyl semimetal state is suggested in these compounds, where the crystal structure becomes a chiral space group $I2_13$ below the structural phase transition [15,49]. Although thermodynamic and transport property measurements of Ce$_{3+x}$Ru$_4$Sn$_{13-x}$ indicate no noticeable structural phase transition below 300 K, a weak superlattice formation shouldn't be neglected because a polycrystalline Ce$_3$Ru$_4$Sn$_{13}$ sample shows signs of a weak structural change in XRD and XPS measurements [26].

IV. SUMMARY

We have grown single crystals of Ce$_{3+x}$Ru$_4$Sn$_{13-x}$ ($0.05 \leqslant x \leqslant 0.34$) with varying Ce/Sn loading compositions, and investigated their physical properties through measurements of EDX, powder x-ray diffraction, electrical resistivity, magnetization, and specific heat. The compound La$_{3.65}$Ru$_4$Sn$_{12.35}$ shows typical metallic behavior down to 2.1 K and undergoes the BCS-type superconducting transition below 2.1 K. For Ce$_{3+x}$Ru$_4$Sn$_{13-x}$, the magnetic susceptibility measurements show that the $4f$ electrons of the Ce^{3+} ions are well localized. The electrical resistivity of Ce$_{3+x}$Ru$_4$Sn$_{13-x}$ follows typical Kondo lattice behavior. Upon increasing x from 0.05 to 0.34, the absolute value of the resistivity increases and the observed minimum temperature moves to higher temperature. While the structural disorder can lead to a significant change in resistivity value as well as the observed temperature dependence, it cannot explain the Kondo lattice behavior observed in this study. At low temperatures, magnetic susceptibility and specific heat show a pronounced broad maximum at $T \sim 3.5$ K for compounds with small x, and the broad maximum disappears as x increases. The maximum cannot be explained by the very simple type of analysis with the Kondo interaction in conjunction with CEF effects. To understand the observed thermodynamic and transport properties of the Ce$_{3+x}$Ru$_4$Sn$_{13-x}$ system, the disordered Ce ions at the $2a$ site and fully ordered Ce ions at the $6d$ sites must be considered.

ACKNOWLEDGMENTS

[1] J. Remeika, G. Espinosa, A. Cooper, H. Barz, J. Rowell, D. McWhan, J. Vandenberg, D. Moncton, Z. Fisk, L. Woolf, H. Hamaker, M. Maple, G. Shirane, and W. Thomlinson, Solid State Commun. **34**, 923 (1980).

[2] J. Hodeau, J. Chenavas, M. Marezio, and J. Remeika, Solid State Commun. **36**, 839 (1980).

[3] B. K. Rai, I. W. Oswald, J. K. Wang, G. T. McCandless, J. Y. Chan, and E. Morosan, Chem. Mater. **27**, 2488 (2015).

[4] M. F. Hundley, J. L. Sarrao, J. D. Thompson, R. Movshovich, M. Jaime, C. Petrovic, and Z. Fisk., Phys. Rev. B **65**, 024401 (2001).

[5] C. S. Lue, H. F. Liu, S.-L. Hsu, M. W. Chu, H. Y. Liao, and Y. K. Kuo., Phys. Rev. B **85**, 205120 (2012).

[6] L. E. Klintberg, S. K. Goh, P. L. Alireza, P. J. Saines, D. A. Tompsett, P. W. Logg, J. Yang, B. Chen, K. Yoshimura, and F. M. Grosche, Phys. Rev. Lett. **109**, 237008 (2012).

[7] U. Köhler, A. P. Pikul, N. Oeschler, T. Westerkamp, A. M. Strydom, and F. Steglich, J. Condens. Matter Phys. **19**, 386207 (2007).

[8] B. K. Rai, I. W. H. Oswald, W. Ban, C.-L. Huang, V. Loganathan, A. M. Hallas, M. N. Wilson, G. M. Luke, L. Harriger, Q. Huang, Y. Li, Sami Dzsaber, Julia Y. Chan, N. L. Wang, S. Paschen, J. W. Lynn, A. H. Nevidomskyy, P. Dai, Q. Si, and E. Morosan, Phys. Rev. B **99**, 085120 (2019).

[9] R. Gumeniuk, Handb. Phys. Chem. Rare Earths **54**, 43 (2018).

[10] B. Eisenmann and H. Schäfer, J. Less-Common Met. **123**, 89 (1986).

[11] M. Schreyer and T. Fässler, Solid State Sci. **8**, 793 (2006).

[12] Y. V. Galadzhun and R. Pöttgen, Z. Anorg. Allg. Chem. **625**, 481 (1999).

[13] K. Ghosh, S. Ramakrishnan, S. K. Dhar, S. K. Malik, G. Chandra, V. K. Pecharsky, K. A. Gschneidner, Jr., Z. Hu, and W. B. Yelon, Phys. Rev. B **52**, 7267 (1995).

[14] V. Anand, D. Adroja, A. Hillier, W. Kockelmann, A. Fraile, and A. Strydom, J. Condens. Matter Phys. **23**, 276001 (2011).

[15] K. Suyama, K. Iwasa, Y. Otomo, K. Tomiyasu, H. Sagayama, R. Sagayama, H. Nakao, R. Kumai, Y. Kitajima, F. Damay, and J. M. Mignot, A. Yamada, T. D. Matsuda, and Y. Aoki, Phys. Rev. B **97**, 235138 (2018).

[16] M. Gamża, W. Schnelle, A. Ślebarski, U. Burkhardt, R. Gumeniuk, and H. Rosner, J. Condens. Matter Phys. **20**, 395208 (2008).

[17] A. Ślebarski, B. D. White, M. Fijałkowski, J. Goraus, J. J. Hamlin, and M. B. Maple, Phys. Rev. B **86**, 205113 (2012).

[18] A. Ślebarski, M. Fijałkowski, J. Goraus, L. Kalinowski, and P. Witas, J. Alloys Compd. **615**, 921 (2014).

[19] V. K. Anand, D. T. Adroja, D. Britz, A. M. Strydom, J. W. Taylor, and W. Kockelmann, Phys. Rev. B **94**, 014440 (2016).

[20] T. Fukuhara, I. Sakamoto, H. Sato, S. Takayanagi, and N. Wada, J. Condens. Matter Phys. **1**, 7487 (1989).

[21] S. Takayanagi, T. Fukuhara, H. Sato, N. Wada, and Y. Yamada, Physica B Condens. Matter **165**, 447 (1990).

[22] V. Anand, D. Adroja, A. Bhattacharyya, A. Hillier, D. Britz, A. Strydom, J. Taylor, A. Fraile, and W. Kockelman, J. Phys.: Conf. Ser. **592**, 012008 (2015).

[23] J. Rodríguez-Carvajal, Physica B Condens. Matter **192**, 55 (1993).

[24] T. Mishra, C. Schwickert, T. Langer, and R. Pöttgen, Z. Naturforsch. B **66**, 664 (2011).

[25] G. P. Espinosa, A. S. Cooper, H. Barz., and J. P. Remeika, Mater. Res. Bull. **15**, 1635 (1980).

[26] A. Ślebarski and J. Goraus, Phys. Rev. B **88**, 155122 (2013).

[27] T. Fukuhara, S. Iwakawa, and H. Sato, J. Magn. Magn. Mater. **104**, 667 (1992).

[28] T. Fukuhara, I. Sakamoto, and H. Sato, J. Condens. Matter Phys. **3**, 8917 (1991).

[29] T. Fukuhara, I. Sakamoto, and H. Sato, Physica B Condens. Matter **165**, 443 (1990).

[30] O. Prakash, A. Thamizhavel, and S. Ramakrishnan, Phys. Rev. B **93**, 064427 (2016).

[31] A. M. Hallas, C. L. Huang, Binod K. Rai, A. Weiland, Gregory T. McCandless, Julia Y. Chan, J. Beare, G. M. Luke, and E. Morosan, Phys. Rev. Materials **3**, 114407 (2019).

[32] H. Ishii, T. Hanyu, T. Fukuhara, I. Sakamoto, H. Sato, and S. Yamaguchi, J. Phys. Soc. Jpn. **62**, 811 (1993).

[33] V. T. Rajan, Phys. Rev. Lett. **51**, 308 (1983).

[34] C. Rossel, K. N. Yang, M. B. Maple, Z. Fisk, E. Zirngiebl, and J. D. Thompson, Phys. Rev. B **35**, 1914 (1987).

[35] N. O. Moreno, A. Lobos, A. A. Aligia, E. D. Bauer, S. Bobev, V. Fritsch, J. L. Sarrao, P. G. Pagliuso, J. D. Thompson, C. D. Batista, and Z. Fisk, Phys. Rev. B **71**, 165107 (2005).

[36] H. Yamamoto, M. Ishikawa, K. Hasegawa, and J. Sakurai, Phys. Rev. B **52**, 10136 (1995).

[37] M. Kratochvílová, J. Prokleška, K. Uhlířová, V. Tkáč, M. Dušek, V. Sechovsky, and J. Custers, Sci. Rep. **5**, 15904 (2015).

[38] E. D. Mun, B. K. Lee, Y. S. Kwon, and M. H. Jung, Phys. Rev. B **69**, 085113 (2004).

[39] M. S. Torikachvili, S. Jia, E. D. Mun, S. T. Hannahs, R. C. Black, W. K. Neils, Dinesh Martien, S. L. Bud'ko, and P. C. Canfield, Proc. Natl Acad. Sci. USA **104**, 9960 (2007).

[40] M. Deppe, S. Hartmann, M. E. Macovei, N. Oeschler, M. Nicklas, and C. Geibel, New J. Phys. **10**, 093017 (2008).

[41] P. Haen, J. Flouquet, F. Lapierre, P. Lejay, and G. Remeny, J. Low Temp. Phys. **67**, 391 (1987).

[42] E. L. Thomas, H.-O. Lee, A. N. Bankston, S. MaQuilon, P. Klavins, M. Moldovan, D. P. Young, Z. Fisk, and J. Y. Chan, J. Solid State Chem. **179**, 1642 (2006).

[43] N. Tsujii, H. Kontani, and K. Yoshimura, Phys. Rev. Lett. **94**, 057201 (2005).

[44] B. Coqblin and J. R. Schrieffer, Phys. Rev. **185**, 847 (1969).

[45] K. Hanzawa, K. Ohara, and K. Yosida, J. Phys. Soc. Jpn. **66**, 3001 (1997).

[46] S. R. Saha, H. Sugawara, T. Namiki, Y. Aoki, and H. Sato, Phys. Rev. B **65**, 214429 (2002).

[47] I. W. Oswald, B. K. Rai, G. T. McCandless, E. Morosan, and J. Y. Chan, CrystEngComm **19**, 3381 (2017)

[48] C. N. Kuo, W. T. Chen, C. W. Tseng, C. J. Hsu, R. Y. Huang, F. C. Chou, Y. K. Kuo, and C. S. Lue, Phys. Rev. B **97**, 094101 (2018).

[49] Y. Otomo, K. Iwasa, K. Suyama, K. Tomiyasu, H. Sagayama, R. Sagayama, H. Nakao, R. Kumai, and Y. Murakami, Phys. Rev. B **94**, 075109 (2016).